A Preprocessor for SSMIS Radiances
Scientific Description

W. Bell

Met Office, UK

This documentation was developed within the context of the EUMETSAT Satellite Application Facility on Numerical Weather Prediction (NWP SAF), under the Cooperation Agreement dated 16 December, 2003, between EUMETSAT and the Met Office, UK, by one or more partners within the NWP SAF. The partners in the NWP SAF are the Met Office, ECMWF, KNMI and Météo France.

Change record				
Version	Date	Author	Approved	Remarks
1.0	31.03.06	W. Bell	S. English (12.06.06)	First Release

Contents

1 Introduction

The first Special Sensor Microwave Imager/Sounder (SSMIS) was launched on the Defense Meteorological Satellite Program (DMSP) F-16 platform on 18th October 2003. In common with its predecessor SSM/I [1], [2] SSMIS employs conical scanning geometry. In general, conical scan geometry offers the advantage that that the polarisation of the measured radiances is invariant across the scan. In addition the open design permits relatively large primary reflectors and consequently affords good horizontal resolution. SSMIS is the first conical scanner to be used for temperature sounding and combines a range of temperature sounding channels (50 - 63 GHz) with humidity sounding channels (183 GHz) as well as a range of imaging channels (19 - 150 GHz). In common with previous conical scanners, however, the open design of SSMIS has several undesirable consequencies. The passive microwave imager on the Tropical Rainfall Measurement Mission (TRMM) satellite, TMI, suffered from thermal emission from the main reflector as described by Wentz *et al* [3] resulting in systematic errors as large as 5K. Twarog *et al* [4] describe the impact of solar radiation on the surface of the external calibration load used in Windsat. These investigations also revealed that similar effects are evident in SSM/I data. Calibration load instabilities have also been investigated in AMSR [5].

The post-launch Cal/Val program revealed that SSMIS also suffers from solar intrusions into the external calibration load and with thermal emission from the main reflector. Both of these effects have been studied and algorithms have been developed to flag or correct affected data, and are implemented in the SSMIS preprocessor described here. It must be emphasised, however, that the refinement of the corrections and the development and improvement of the physical models undepinning them is ongoing. This development work is being undertaken by a number of groups forming the extended Cal/Val team for SSMIS. It is planned that a final version of the pre-processor, incorporating the best algorithms from this wider research and development effort, will be incorporated into the existing ground processing segment currently run at Fleet Numerical Meteorological Operations Centre (FNMOC) in Monterey, US. The pre-processor described here is, therefore, a particular implementation of the specific correction algorithms developed at the UK Met Office to allow users at NWP centres to generate useful data from the currently available F-16 SSMIS data stream. The long term intention is that the best of the methods described here are refined and incorporated into the pre-processor to be run at FNMOC.

By design SSMIS oversamples the upwelling radiance field in the along track direction. In addition, the short integration time per obsevation (4 ms) has the consequence that the random noise is relatively large for many channels. Set against this, the accuracy requirements defined by radiance assimilation applications for temperature sounding channels are very demanding. Typical background equivalent noise figures for current global NWP models are conservatively estimated to be in the range 0.2 - 0.4K for tropospheric temperature sounding channels. Routine monitoring of innovations (or first guess departures) computed from AMSU-A radiances using background fields from the Met Office global model are in the range 0.1 - 0.2K for the tropospheric sounding channels, suggesting the quality of background fields is, in reality, closer to 0.1K. It might be expected, therefore, that radiances should have uncertainties of the order of 0.2 K or better to improve the analysis, and hence improve forecast quality.

The SSMIS data stream comprises data from the four instrument subtypes on SSMIS each associated with a subset of the total of 24 SSMIS channels: the lower atmospheric sounding channels (LAS); the upper atmospheric sounding (UAS) channels; the imaging (IMA) channels and the environmental (ENV) channels. These data streams are produced from seperate feeds on SSMIS and are not co-located. This can present problems for some assimilation systems, for example when a low model top requires that temperatures above model top (that affect channels with lower peaking weighting functions) are extrapolated using measured brightness temperatures from higher peaking channels. Non co-location can also cause problems where there is a need to determine cloud liquid water paths from the data in order to screen cloud affected radiances, requiring that cloud sensitive window channels are co-located with temperature sounding channels.

This document aims to describe these issues and the approaches used to deal with them in the SSMIS preprocessor. These issues define the four main functions of the SSMIS preprocessor :

- Remapping the data to a common grid;
- Averaging the data over (variable) spatial scales;
- Flagging observations that are affected by solar intrusions into the warm calibration load
- Correcting the observations for thermal emission from the main reflector.

Following on from an overview of the instrument in Section 2 these issues define the contents of Sections 3-6 re-specively. In Section 7 the performance of the pre-processor is described, in terms of the statistics of innovations obtained using the Met Office model, and also in terms of impact on forecast quality in the Met Office global model.

In section 8 the outstanding issues and priorities future research and development work are described.

2 Instrument description

The SSMIS is shown in Figure 1. The main paraboloidal reflector is 0.6m in diameter and rotates about a vertical axis at 30 rpm. The reflector is inclined at approximately 23 degrees to the horizontal. Upwelling radiance is focussed onto an up-looking feedhorn array which is fixed relative to the main reflector. This arrangement results in a beam direction of 45 degrees to nadir at the spacecraft (see Figure 2). From the orbit altitude of 859 km the curvature of the earth results in a local earth incidence angle of approximately 53 degrees. There are two benefits of this particular earth incidence angle. Firstly, over ocean the windspeed dependence of the surface emissivity for vertically polarised radiances is a minimum, so that the difference between emissivities for horizontally and vertically polarised channels at a given frequency is a simple function of windspeed. Secondly, in calculating the contribution to top-of-atmosphere (TOA) measured radiances from surface scattering the sensitivity to the chosen scattering model (*eg* lambertian *vs* specular) is low [8] .

A two point radiometric calibration is obtained every scan line. Once per rotation of the main reflector the feedhorns pass under the warm calibration load and then under a cold space reflector. The warm calibration load comprises pyramidal structures (*tines*) maintained at a fixed temperature of 306K. The tines are constructed from aluminium coated in highly emissive paint. The warm load is in principle, to a good approximation, a black body at fixed and known temperature.

An array of feedhorns in the focal plane of the reflector collect focussed radiation from the main reflector. Each feedhorn serves a group of channels. A consequence of the non-colocation of the feedhorns is that the beams for each channel subset are not colinear and hence the ground footprints are not colocated.

SSMIS has 24 channels in total, the specificiation of these channels for F16 SSMIS is given in Table 1. The channels are grouped into four instrument sub-types corresponding to the lower atmopsheric sounding (LAS) channels, the upper atmospheric sounding (UAS) channels , the imaging (IMA) channels and the environmental (ENV) channels. It should be noted that the polarisation for channels 1-5 was planned to be horizontal, however post-launch tests showed that the final alignment of the feedhorns gave vertical polarisation. For assimilation purposes this requires that fast radiative transfer models (eg RTTOV) have coefficient files amended accordingly. Future sensors may have the polarisation for these channels reset to vertical as originally planned.

Four further SSMIS instruments (F17 - F20) are planned for launch during the period 2006-2011, giving good operational continuity to 2015 and, probably, beyond. All of these sensors are scheduled to go into early moring or near-terminator orbits.

The current version of the pre-processor takes as input bufrised versions of the *Temperature Data Records* produced at Fleet Numerical Meteorology Operations Centre (FNMOC). These brightnes temperatures are effectively antenna temperatures and have not been corrected for *spillover*. Spillover arises because the field of view of the instrument feedhorns overfill the main reflector and consequently the feedhorn measured brightness temperature has a contribution from cold space. The spillover correction is implemented in the SSMIS preprocessor described here. It is anticipated that in future the spillover corrections, and the antenna emission correction described below, will be carried out at source (at FNMOC), and the funcionality of the pre-processor will be modified in order that it carries out only remapping and averaging of the radiances.

3 Remapping

As discussed in Section 2, the four instrument subtypes for SSMIS have non-colocated footprints. A section of the SSMIS swath is shown in Figure 3. The distance between adjacent scanlines is 12.5 km. From Table 1 it can be seen that the 3 dB footprints for all channels are such that the radiance field is heavily oversampled in the along track direction (see Figures 3 and 4). Remapped data offers the benefits of simpler and more reliable cloud detection, and also enables high peaking channels to be used to extrapolate temperatures above the model top. For these reasons the SSMIS brightness temperatures are remapped in the pre-processor to the grid defined by the LAS observations. This is done by using pre-computed interpolation coefficients.

Firstly, each subtype brightness temperature data set is defined within a 2D array indexed by scan line (l) and scanposition (p) . For each of the 60 LAS fields of view, the four nearest neighbours for each of the other scan types (UAS, IMA and ENV) are used to construct the brightness temperature at the LAS footprint location. For each channel, for each LAS footprint location, a weighted average of the four nearest neighbour radiances is computed (see Figure 5). For example the UAS brightness temperatures (T_B^{UAS}) remapped to the LAS footprint are given by:

$$T_B^{LAS}(l,p) = \sum_{i=1}^{4} w_i^{UAS}(p) T_B^{UAS}(l+\delta_i(p), p_i'(p)) \tag{1}$$

Where:

$T_B^{LAS}(l,p)$ is the value of the (UAS) brightness temperatures at the LAS location indexed by scanline l and scan position p.

$w_i^{UAS}(p)$ is the weighting attached to (UAS) neighbour i to LAS scan position p.

$T_B^{UAS}(l+\delta_i(p), p_i'(p))$ is the value of the UAS channel brightness temperatures at UAS footprint location indexed by scan line $(l+\delta_i(p))$ and scan position $p_i'(p)$, where $\delta_i(p)$ is an offset from the LAS scan line (l) which is precomputed for each of the four neighbours for each of the 60 LAS scan positions, and $p_i'(p)$ is the absolute scan position of the UAS footprint which is the i th nearest neighbour to the LAS footprint at scan position p.

The weights $w_i^{UAS}(p)$ are given by the inverse distance between the LAS points at index (l,p) and the neighbouring UAS points indexed by $(l+\delta_i(p), p_i'(p))$:

$$w_i^{UAS}(p) = C||(l,p),(l+\delta_i(p),p_i'(p)||^{-1} \tag{2}$$

where $||(a,b),(c,d)||$ is the (great circle) distance betwen points labelled by scan line, scan position index pairs (a,b) and (c,d). All of the relative indices ($\delta_i(p)$ and $p_i'(p)$) as well as the weights ($w_{UAS}^i(p)$) are invariant with scan line and can be pre-computed from a small section of orbit. C is an appropriate normalisation constant, such that:

$$\sum_{i=1}^{4} w_i^{UAS}(p) = 1 \tag{3}$$

4 Data Averaging

SSMIS oversamples the brightness temperature field at high noise. Random noise amplitudes were estimated from the measurements by computing distibutions of standard deviations of the brightness temperatures in the central fifteen fields of view for the lower atmospheric sounding channels. This can be used to estimate the random noise component in the measured radiances. Figure 6 shows the distribution for channel 4 and, for comparison, the distribution computed from a synthetic flat field with added random noise. The results for the lower atmospheric sounding channels are shown in Table 2. A calculation of $\mathbf{HBH^T}$ gives values in the range 0.2 - 0.4K for these channels. The (**B**) used in this calculation is that used in the Met Office 1D Var pre-processing system and is an approximation to the full error covariances used in 4D Var. $\mathbf{HBH^T}$ can be used as a measure of the quality of radiances required to significantly improve the analysis. As can be seen from Table 2, the random noise component alone for several lower atmospheric sounding channels is comparable to $\mathbf{HBH^T}$.

For each six hour assimilation window approximately 682 000 SSMIS observations are available. In most NWP assimilation systems it is common practise for large volumes of satellite data to be reduced by spatial thinning prior to assimilation, however, in the case of SSMIS this would result in unacceptably high levels of random noise. There is, therefore, significant benefit in averaging the data prior to spatial thinning. Superobbing, as defined in Lorenc *et al* [6], involves averaging innnovations over a specified domain. In the case of spatial domains within which the variation of the background field is linear, averaging observations is equivalent to averaging innovations. For the case of temperature sounding channels for which the horizontal spatial scales of atmospheric features are generally large, then large domains (100 - 300 km) can be chosen for which the background variation remains linear to a good approximation.

Two approaches to averaging the brightness temperature fields were considered. In the first, the averaging was carried out in the spectral domain. In this approach the brightness temperatures are defined on a two dimensional grid indexed by scan line and scan number. This is then transformed to the spectral domain by carrying out a two dimensional fast fourier transform (FFT) on the field. High frequency components can be attenuated using a gaussian weighting and the inverse transform can then be carried out to recover a smoothed brightness temperature field. A drawback of this approach is that edge effects make it difficult to define sensible effective averaging functions near the edge of the swath. A second approach, which was adopted in the end, used simple averaging over circular domains centred on each field of view. The advantage of this approach is that it is simpler to implement. In common with the spectral approach described above, it also suffers from distortion of the averaging functions near the edge of the swath. The implementation is simply an extension to the approach developed for the data remapping described above. Following the notation described in Section 3, the average brightness temperature field (T_B') is computed from the original remapped brightnes temperature field (T_B) as follows:

$$T_B'(l,p) = \sum_{i=1}^{N} w_i(p) T_B(l + \delta_i(p), p_i'(p)) \tag{4}$$

where:

$$w_i(p) = \exp(-\frac{r_i^2}{2\sigma^2}) \tag{5}$$

and

$$r_i = \|(l,p),(l+\delta^i(p),p_i'(p)\| \tag{6}$$

N is the domain size in terms of number of nearest neighbours used fro averaging and has been chosen to be 200. The improvement in noise is illustrated in Figure 7. A target level of noise reduction of 0.33 (to bring LAS random noise below 0.1K) is achieved for averaging scales given by $\sigma = 25$km. This corresponds to a FWHM for the averaging function of 58.9km.

5 Solar Intrusions and Gain anomalies

An initial evaluation of the data gave unexpectedly large variances for the computed innovations for the LAS temperature sounding channels (2-7,23,24). Figure 8 shows the innovations computed for these channels. For channels 4-6 the standard deviations of the computed innovations is in the range 0.5 - 0.8K. Allowing for the (pre-averaging) noise contribution of 0.3K and the known background field quality (0.1- 0.2K for these channels) there is evidence for an additional source of error contributing to the observed variance in the innovations.

The instrument data stream contains the onboard calibration data comprising measured warm load temperature, cold scene counts and warm load counts. This data can be used to compute the gain for each channel for each scan line. A time series of this data is shown for channel 6 in Figure 9 alongside a time series of smoothed innovations. As can be seen from Figure 9, positive anomalies in the gain time series correspond to negative anomalies in the innovation time series.

Investigations during the post-launch Cal Val program showed that these anomalies were due to solar radiation striking the surface of the warm load tines. This results both from direct solar intrusions, and from sunlight reflected from the highly reflective top deck of the instrument. These intrusions occur typically 3 - 4 times per orbit and are of 5-10 minutes duration. The exact phasing of these effects varies throughout the year as the angle of the orbit plane relative to the solar vector changes. The impact on the lower atmospheric temperature sounding channels is 1.0 - 1.5K in magnitude and is therefore a very significant effect for tropospheric temperature sounding channels.

As an initial approach it was decided to flag and reject data affected by solar intrusions. This was achieved by constructing a climatological map of the solar intrusions. This was done by carrying out some simple signal processing of the gain time series. Computing the second derivative of the gain time series with respect to time has the effect of isolating the relatively fast variations in gain resulting from the solar intrusions from the slower true variation of the gain around the orbit (see Figure 10). A threshold can be applied to the derivative time series to identify regions affected by intrusions. This is then used to construct a map of where the intrusions occur in the two dimensional space defined by the local solar zenith and azimuth angles. This approach is effective in identifying the location of the peak of the solar intrusions. In order to allow for the temporal extent of the intrusions, the initial map is *blurred* by a two dimensional gaussian convolution. An example of the resulting map is shown in Figure 11. The perfomance of the map in flagging intrusions is shown for two sections of data in April and June 2005. A drawback of the intrusion mapping is that 30 - 40 % of the data is flagged and subsequently not used each orbit.

Alternative approaches, based on fourier filtering the gain time series to construct an estimate of the true gain variation have been used with some success [7] and it is likely that in the near future operational data streams based on these corrections will become available.

6 Reflector Emission

The main reflector of SSMIS is a 60 cm diameter off-axis paraboloid fabricated from graphite epoxy honeycomb. This honeycomb substrate material is coated in vacuum deposited aluminium to give a highly reflective surface and this in turn is coated with vacuum deposited non-stoichiometric SiO_x for resilience. The SiO_x is approximately 1 micron in thickness. Pre-launch tests of the main reflector gave measured reflectivities of 0.9999. It appears that on orbit, however, the main reflector has become emissive. It is hypothesised that this is a result of degradation of the SiO_x coating during lengthy launch delays during which SSMIS was stored in relatively high humidity environments. This can result in absorption of water onto the SiO_x coating resulting in reduced reflectivity and consequently significant emissivity. Once per orbit the instrument enters earth shadow for a period of approximately 10 minutes. During this time the reflector cools by 80K. This thermal cycling, coupled with the emissive reflector results in the superposition of a thermal emission signal on the measured scene brightness temperatures.

Further analysis by the Cal/Val team of the orientation of the instrument relative to the sun revealed that just prior to entering earth shadow, and again immediately after exiting earth shadow, the main reflector is subject to direct solar illumination at steep incidence angles. This results in significant warming of the reflector prior to and, more particularly, immediately afer emergence from earth shadow.

The effect of this emission on the measured radiances is illustrated in Figure 12 which shows the global map of innovations for channel 6 computed for a 12 hour period. The reflector emission effects are most manifest on the northbound ascending node of the orbit, at approximately 10° North, where the innovations show an almost instantaneous increase of 1.5K. Figure 13 shows the evolution of the innovations for channel 4 as a time series round the orbit. In this plot the innovations have been smoothed to emphasise the systematic variations. On emergence from earth shadow the reflector temperature appears to increase by 80K over a period of less than 10 minutes. Simultaneously the observations increase by 1.0K.

In principle the effect of the thermal emission from the main reflector can be calculated. The scene temperature (T_{scene}) can be constructed from the observed brightness temperature (T_{obs}) as follows:

$$T_{scene} = \frac{T_{obs} - K\varepsilon T_{ref}}{K(1-\varepsilon)} \tag{7}$$

The unknowns to be determined are the temperature of the main reflector (T_{ref}) and the effective emissivity (ε) of the reflector for each channel, neither of which is avaialble directly from measurements. The emissivity is potentially frequency and polarisation dependent. K is the spillover correction for each channel. These are estimated empirically by iteratively adjusting until the computed innovations for each channel give a global mean of zero. From equation (7) the required accuracy in the determination of T_{ref} (ΔT_{ref}) and the emissivity ($\Delta\varepsilon$) to achieve a specified tolerable error in T_{scene} (ΔT_{scene}) are computed. The results are summarised in Table 3.

Temperature measurements are available from a sensor placed on the rim of the main reflector, close to the support arm. Investigations showed that the measured arm temperatures are not sufficiently accurate estimates of the reflector face temperature itself. Reflector emission corrections based on the arm temperature produced residuals of 0.5 K in innovations in the region of emergence from Earth shadow. An empirical reflector temperature was constructed from the measured arm temperature (T_{arm}) data as follows:

$$T_{ref}(t) = T_{arm}(t) + c\frac{dT_{arm}}{dt}(t) \tag{8}$$

Where the second term on the RHS can be thought of as a correction to the measured arm temperature where the magnitude of the correction is determined by the parameter c. The derivative of the arm temperature with respect to time is generated numerically using the forward difference approximation, with appropriate smoothing applied to both

the original arm time series and the resulting derivative. Subsequently, it was found that near zero innovations could only be obtained by additionally *lagging* the correction term :

$$T_{ref}(t) = T_{arm}(t) + c_1 \int_0^T c_2 e^{-\tau/\sigma} \frac{dT_{arm}}{dt}(t-\tau)d\tau \tag{9}$$

Where c_2 normalises the exponential lagging function over the interval $[0, T]$. T is typically 30 minutes, σ defines the width of the lagging function and typically takes values in the range 2 - 10 minutes.

The effective emissivities of each channel and the scale factor (c_1) used to scale the correction term in equation 9 were determined by fitting the innovations for a single assimilation cycle. The results for the temperature sounding channels 2 - 7, the moisture sounding channels 9-11, and the imaging channels 12-16 are shown in Figure 14. The apparent polarisation dependence of the effective emissivity is illustrated by the difference betwen channels 2 - 5 (emissivities close to 0.01) and chanels 6 and 7 (effective emissivities close to 0.02). It was found that for the SSMI-like imaging channels the effective emissivity is close to 0.00 and for the 183 GHz channels is in the range 0.035 - 0.045 (see Table 4). Due to greater uncertainties in the background fields for the quantities influencing these channels and the greater uncertainties in the radiative transfer modelling for these channels the reproducibility of the results obtained using this technique is worse than for the lower atmospheric sounding channels.

6.1 Physical basis for reflector emission correction

The physical basis for the empirical reflector emission correction can be investigated by considering the heat transfer equation governing the time evolution of the measured arm temperature:

$$a_1 \frac{dT_{arm}}{dt} = a_2 f(t) - a_3 (T_{arm}^n - T_0^n) \tag{10}$$

Where $f(t)$ captures the time evolution of the solar radiative forcing function, and the second term on the RHS is a *sink* term where n takes the value of 1 if the arm cools conductively to a sink at temperature T_0 , and takes the value 4 if the dominant cooling mechanism is radiative. The constants $a_{1,2,3}$ are related to the heat capacity, geometry and thermal conductivity/emissivity of the arm respectively. During the part of the orbit where the spacecraft is in Earth shadow, the solar radiative forcing term is zero and the numerically computed derivative ($\frac{dT_{arm}}{dt}$) can be plotted against T_{arm}^n for the values $n = 1, 4$. Figure 15 shows the resulting plot for $n = 1$. From this it can be concluded that the arm cools conductively ($n = 1$) to a sink at a temperature of approximately 217K. Equation 10 can then be rearranged to express the (scaled) solar forcing as follows:

$$\frac{a_2}{a_3} f(t) = (T_{arm} - T_0) + \frac{a_1}{a_3} \frac{dT_{arm}}{dt} \tag{11}$$

ie a scaled representation of the solar radiative forcing throughout the orbit can be constructed from the arm temperature data. The form of this derived forcing function is shown in Figure 16. There is good qualitative agreement between the form of this solar forcing and the form computed based on the spacecraft and orbit geometry , particularly in the regions prior to the spacecraft entering Earth shadow and immediately following emergence from Earth shadow.

If it can be assumed that the reflector face also cools conductively, then the problem of determining the reflector temperature reduces to determining the solution of an equation similar to equation 10, with the forcing term given by equation 11

$$b_1 \frac{dT_{ref}}{dt} = b_2 f(t) - b_3 (T_{ref} - T_0) \tag{12}$$

As the constants b_1,b_2 and b_3 , are related to the (unknown) thermal properties of the reflector it is not possible at this time to compute the solutions to equation 12 , but it can be solved numerically by fitting the form of solution to that given by the empirical temperature correction, in order to demonstrate that the empirical form of the reflector temperature is consistent with the solution of the heat transfer equation for *some* choice of thermal properties. A comparison of the derived reflector temperatures for both empirical and physical approaches in shown in Figure 17. The difference between the two forms is mostly within the 5K accuracy requirement but there is a discontinuity resulting from correctable residual edge effects in the empirical correction. Work is ongoing to reconcile these estimates of the antenna temperature with a fully physical solution to Equation 12 based on reasonable estimates of the thermal properties of the reflector.

Recent work at NRL (S. Swadley, *private communication*) has further refined the reflector emission correction by taking account of the additional radiative forcing from the Earths outgoing longwave radiation. Initial studies suggest this forcing might restrain the cooling of the reflector in the region of Earth shadow.

The final emissivities for each of the 24 SSMIS channels are given in Table 4.

7 Performance

Figures 18 and 19 show the uncorrected and corrected brightness temperature time series over a single assimilation cycle for channels 2-5 and channels 6,7,23 and 24 respectively. The performance of the pre-processor is best for channel 4 (54.4 GHz). The time series plots for channels 5,6 and 7 still show residual biases in the region of emergence from earth shadow for reasons that are not fully understood. Further work is required to further refine the reflector emission corrections applied for these channels and possible approaches are described in Section 8.

7.1 Global Innovation Statistics

The SSMIS pre-processor has been run in a semi-operational test mode since August 2005 in order to establish the performance of the pre-processor and the robustness of the data stream. The radiances were compared against background radiances (or First Guess radiances) from the Met Office operational global model. Four times per day (00Z, 06Z, 12Z and 18Z) SSMIS observations obtained over a six hour assimilation window were compared with background radiances. Bias corrections were applied to the SSMIS radiances using a predictor - corrector scheme in which predictors based on 850-300 hPa, and 200-50 hPa thicknesses were used in addition to a constant offset for each channel. The results are summarised in Figures 20 and 21 over the period February - April 2006. The mean biases and standard deviations over this period are shown in Table 5. For the tropospheric sounding channels with relatively small contributions from the surface (channels 3 and 4) the mean standard deviation of the innovations is below 0.2K, at 0.179K and 0.156K respectively, during this period. For the lower peaking channel 2 over ocean the standard deviation is slightly higher at 0.235K, as might be expected from the larger contribution from the (more uncertain) ocean surface emission/reflection. The mean standard deviation for channel 5 is 0.272K and for channels 6 and 7 is higher still at 0.474K and 0.465K as a result of inaccuracies in the antenna emission corrections for these channels.

Figure 22 shows the number of observations processed for each 6 hour window for the period February - April 2006. Normally, for a 6 hour assimilation window 682,000 observations are available. The intermittant outages (eg mid-February 2006) are a consequence of technical problems in the 1D Var processing of the data using non-operational queues, or local storage problems. Typically 40-60 % of the observations pass a 1D Var quality control stage, with a large percentage (30-40%) rejected as a result of rain/intrusion flagging. A total moisture control variable, incorporating both vapour and liquid phase water, is used in the 1D Var analysis and this can cause convergence problems for profiles close to saturation. This results in the rejection of approximately 10% of the observations.

7.2 Assimilation Trials

Two assimilation tests were carried out using data generated using the pre-processor. In the first experiment (2SAT+SSMIS) the impact of the SSMIS temperature sounding channels was tested against a system in which the AMSAU-A instrument data from two NOAA satellites was included (NOAA-16 and NOAA-18). This experiment was aimed at investigating the impact of SSMIS on a system with no temperature sounding data from an AMSU-A instrument in a morning orbit (*eg* as the result of the loss of AMSU-A on NOAA-15). In the second experiment (3SAT+SSMIS) SSMIS was addded to a system including three NOAA AMSU-A instruments, to simultate the impact of adding SSMIS to a full operational system.

Both experiments were run using 3D-Var, using an N216 (*ie* spectral truncation above wave 216) version of the Met Office global model. The results are summarised graphically in Figures 23 and 24. For both experiments the most significant impacts are in the southern hemisphere where RMS errors for Day 1-3 PMSL for both trials are improved by 1 - 2.5%. Elsewhere the impacts are near neutral. The observation errors assumed in these trials were 0.5K for channels 2-5 and 1.0K for channels 6,7,23 and 24.

8 Future Work

There are several areas where further development work is required to improve the quality of SSMIS radiances:

- ***Refinements in the reflector emission correction***. There are still outstanding problems with the performance of the reflector emission corrections applied to channels 5-7,23 and 24. There is also uncertainty over the physical basis for the discontinuity in the effective emissivities between channels 2-5 and channels 6 and 7 (S. Swadley, *prvate communication*). The justification for the empirically constructed reflector temperature presented here is based on the similarity between the form of the constructed reflector temperature and the form of solutions to the heat transfer equation using a solar solar radiative forcing function constructed from measured temperature data. Recent work at the Naval Research Laboratory (NRL) has shown that although this approach correctly accounts for the form of the solar forcing, in the region of earth shadow the reflector is subject to additional forcing from upwelling long wave radiation which may limit the cooling of the reflector in Earth shadow. Modified empirical reflector temperatures, taking into account this forcing, are currently being evaluated at NRL. Reconciling these optimised empirical reflector temperatures with solutions to the heat transfer equation which take account of the solar forcing *a*nd the long wave radiative forcing should provide a physically based algorithm which can be used for correcting radiances from F-16 SSMIS and later flight models if necessary.

- ***Recovery of intrusion flagged data***. Gain correction algorithms have been developed by the instrument manufactureres (Northrop Grumann) and are currently under evaluation at NRL. This algorithm is based on a fourier analysis of the measured gain timeseries in which high frequency variations, due to the solar intrusions, are truncated in a reconstruction of the gain. Similar algorithms have been developed at NOAA/ NESDIS (see [7]) and are under evaluation at the Joint Centre for Satellite Data Assimilation. When a data stream of gain corrected brightness temperatures becomes available from NRL/FNMOC the pre-processor described here would require a simple change to the solar intrusion map to test these radiances (the intrusion map would be set to zero for all local zenith and azimuth angles).

- ***Assessment of quality of the imaging and moisture sounding channels***. Efforts to date have focussed on a detailed study of the quality of the radiances in the temperature sounding channels where radiometric accuracy is most critical. As a next step a detailed study of the quality of the SSMI-like and the AMSU-B like channels will be undetaken, including an assessment of the impact of assimilating radiances from these channels.

- ***Improvements to the remapping scheme for the imager channels***. The current remapping scheme remaps all instrument sub-channel radiances to the LAS grid. Although the imager channels are oversampled and the RMS distance between LAS footprint centres and the four nearest IMA neighbours used in the remapping is approximately 5km it is possible that the effective *interpolation* of precipitation affected radiances will cause problems for some NWP applications. At the review stage in the testing of the preprocessor it has been sugggested that future versions of the preprocessor offer the capability to map the LAS, UAS and ENV radiances to the IMA grid.

References

[1] J. P. Hollinger, J.L.Pierce and G.Poe, SSM/I instrument evaluation, *IEEE Trans. Geosci. Remote Sensing*, Volume 28, Issue 5, (September 1990), pp. 781-790.

[2] M. C.Colton and G.A Poe, Intersensor Calibration of DMSP SSM/I's F-8 to F-14 1987-1997, *IEEE Trans. Geosci. Remote Sensing*, Volume 37, (January 1999), pp. 418-439.

[3] F. J. Wentz, P. Ashcroft and C. Gentemann, Post-Launch Calibration of the TRMM Microwave Imager, *IEEE Trans. Geosci. Remote Sensing*, Volume 39, Issue 2, (February 2001), pp. 415-422.

[4] E. M. Twarog, W. E. Purdy, P. W. Gaiser, K. W. Cheung and B. E. Kelm, WindSat On-Orbit Warm Load Calibration, *IEEE Trans. Geosci. Remote Sensing*, Volume 44, Issue 3, (March 2006), pp 516-529.

[5] K. Imaoka, Y. Fujimoto, M. Kachi, T. Takeshima, T. Igarashi, T. Kawanishi, and A. Shibata: Status of calibration and data evaluation of AMSR on board ADEOS-II. *SPIE Int'l Symposium, Remote Sensing Europe,Barcelona, Spain, 2003*

[6] A. C. Lorenc, A Global Three Dimensional Multivariate Statistical Interpolation Scheme, 1981, *Monthly Weather Review*, Volume 109, 1981, pp 701-721.

[7] B. Yan, F. Weng and N. Sun, Assesssments of F16 Special Sensor Microwave Imager and Sounder (SSMIS) Data for NOAA Operational Applications, Proceedings of Microwave Radiometry and Remote Sensing Applications conference , San Juan , Puerto Rico, 2006.

[8] C. Matzler and P. W. Rosenkranz, Dependence of Brightness Temeprature on Biastatic Scattering with Applications to Antarctica, Proceedings of Microwave Radiometry and Remote Sensing Applications Conference, San Juan , Puerto Rico, 2006.

9 Tables and Figures

Channel Number	Frequency GHz	RF Bandwidth MHz	Pol	3dB footprint km	Sample Spacing km	NEΔT at 305K / K	Subtype
12	19.35	355.0	H	46.5×73.6	25	0.35	ENV
13	19.35	356.7	V	46.5×73.6	25	0.34	ENV
14	22.235	407.5	V	46.5×73.6	25	0.45	ENV
15	37.0	1615	H	31.2×45.0	25	0.26	ENV
16	37.0	1545	V	31.2×45.0	25	0.22	ENV
1	50.3	380.0	V	37.7×38.8	37.5	0.21	LAS
2	52.8	388.8	V	37.7×38.8	37.5	0.20	LAS
3	53.596	380.0	V	37.7×38.8	37.5	0.21	LAS
4	54.40	382.5	V	37.7×38.8	37.5	0.20	LAS
5	55.50	391.3	V	37.7×38.8	37.5	0.22	LAS
6	57.29	330.0	RC	37.7×38.8	37.5	0.26	LAS
7	59.4	238.8	RC	37.7×38.8	37.5	0.25	LAS
24	$60.79 \pm 0.36 \pm 0.050$	106.0	RC	37.7×38.8	37.5	0.38	LAS
23	$60.79 \pm 0.36 \pm 0.016$	29.28	RC	75.2×75.0	75	0.37	UAS
22	$60.79 \pm 0.36 \pm 0.0055$	10.48	RC	75.2×75.0	75	0.58	UAS
21	$60.79 \pm 0.36 \pm 0.002$	5.16	RC	75.2×75.0	75	0.86	UAS
19	63.28 ± 0.28	2.72	RC	75.2×75.0	75	1.23	UAS
20	60.79 ± 0.36	2.70	RC	75.2×75.0	75	1.18	UAS
17	91.655 ± 0.9	2836	V	13.2×15.5	12.5	0.19	IMA
18	91.655 ± 0.9	2822	H	13.2×15.5	12.5	0.19	IMA
8	150.0 ± 1.25	3284	H	13.2×15.5	12.5	0.53	IMA
9	183.31 ± 6.6	1025	H	13.2×15.5	12.5	0.56	IMA
10	183.31 ± 3.0	2038	H	13.2×15.5	12.5	0.39	IMA
11	183.31 ± 1.0	3052	H	13.2×15.5	12.5	0.38	IMA

Table 1: Channel specifications for F-16 SSMIS. The NEΔT specifications are based on pre-flight tests and assume along track averaging.

Channel	Estimated noise (1 σ) /K
1	0.35
2	0.32
3	0.30
4	0.29
5	0.31
6	0.40
7	0.45
24	0.66

Table 2: Estimated noise figures for LAS channels.

Channel	Frequency / GHz	Polarisation	ΔT_{scene} / K	ε_{nom}	$\Delta\varepsilon$	ΔT_{ref} / K
1 - 5	50.3 - 55.5	V	0.1	0.01	0.0008	10.0
6 - 7,19 - 24	57.3 - 63.3	LC	0.1	0.02	0.0010	5.0
9 - 11	183.31	H	0.5	0.04	0.0060	12.0
12 - 16	19.4 - 77.0	V/H	0.5	0.00	-	-

Table 3: Required accuracy in the estimate of reflector emissivity and temperature (ΔT_{ref} and $\Delta\varepsilon$) for a specified tolerable error in T_{scene} (ΔT_{scene}) using sensitivities computed from Equation 7 and assumed nominal emissivities.

Channel	Spillover correction	Effective emissivity
1	0.980	0.01
2	0.985	0.01
3	0.988	0.01
4	0.989	0.01
5	0.985	0.01
6	0.9752	0.02
7	0.9798	0.02
8	0.9949	0.04
9	0.9934	0.04
10	0.9934	0.04
11	0.9934	0.04
12	0.950	0.00
13	0.960	0.00
14	0.9820	0.00
15	0.9810	0.00
16	0.9850	0.00
17	0.9820	0.03
18	0.9780	0.05
19	0.9713	0.02
20	0.9713	0.02
21	0.9713	0.02
22	0.9713	0.02
23	0.9713	0.02
24	0.9713	0.02

Table 4: Spillover corrections and assumed effective emissivity for SSMIS channels 1-24.

Channel	MEAN (O-B) / K	STDEV (O-B) /K
2	0.115	0.235
3	0.084	0.179
4	0.076	0.156
5	0.025	0.272
6	-0.159	0.474
7	-0.101	0.465
9	0.108	1.644
10	0.175	1.894
11	0.414	2.467
12	-0.808	2.874
13	-0.391	1.563
14	-0.432	2.340
15	-1.271	3.761
16	-0.605	1.859
17	-0.470	2.224
18	-1.564	5.717
23	-0.082	0.881
24	-0.185	0.828

Table 5: Biases and standard deviations of pre-processed, quality controlled and bias corrected SSMIS radiances during the period 1st February - 1st May 2006.

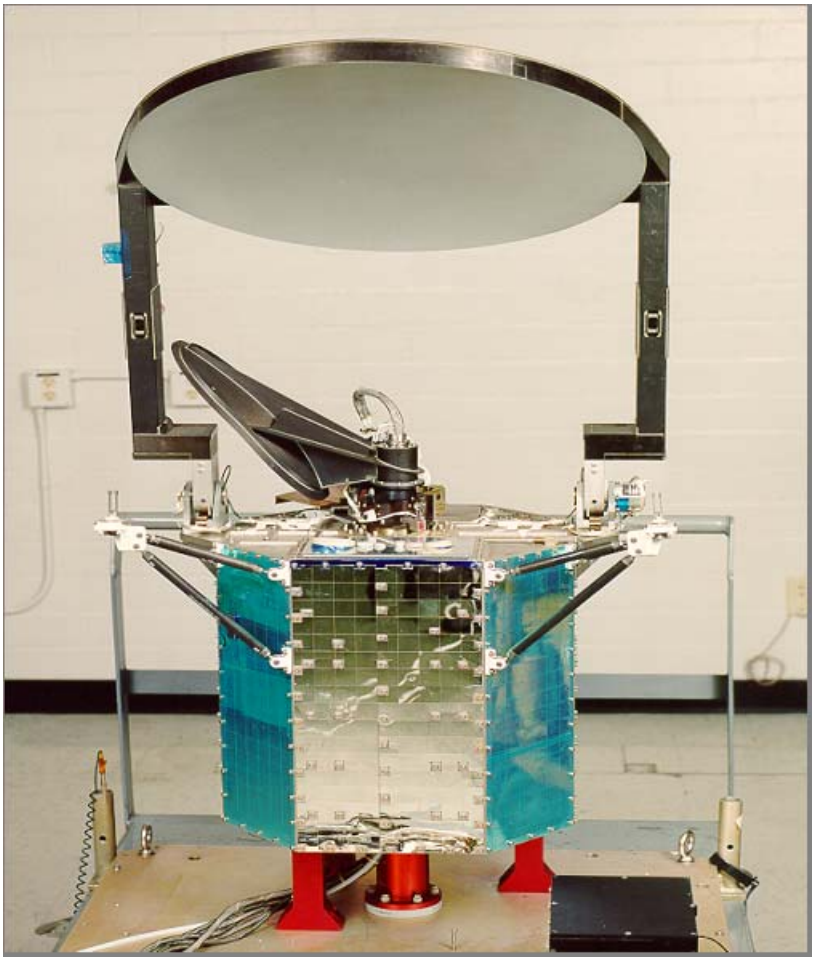

Figure 1: The Special Sensor Microwave Imager/Sounder (SSMIS).

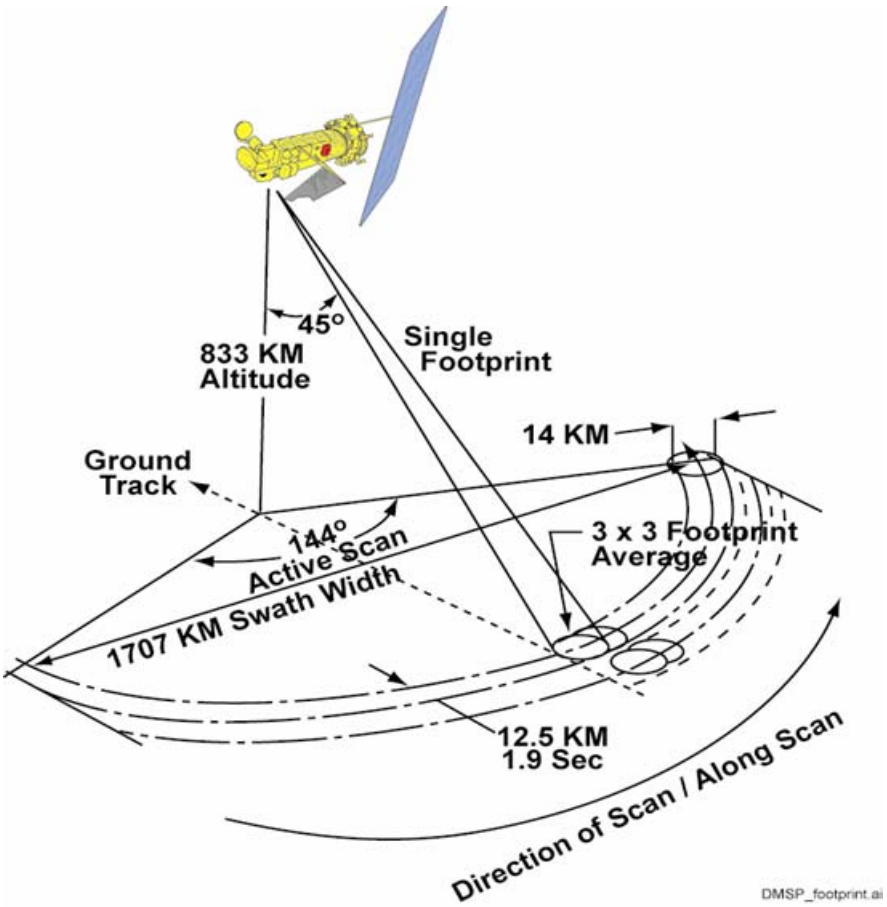

Figure 2: Conical scan geometry of SSMIS.

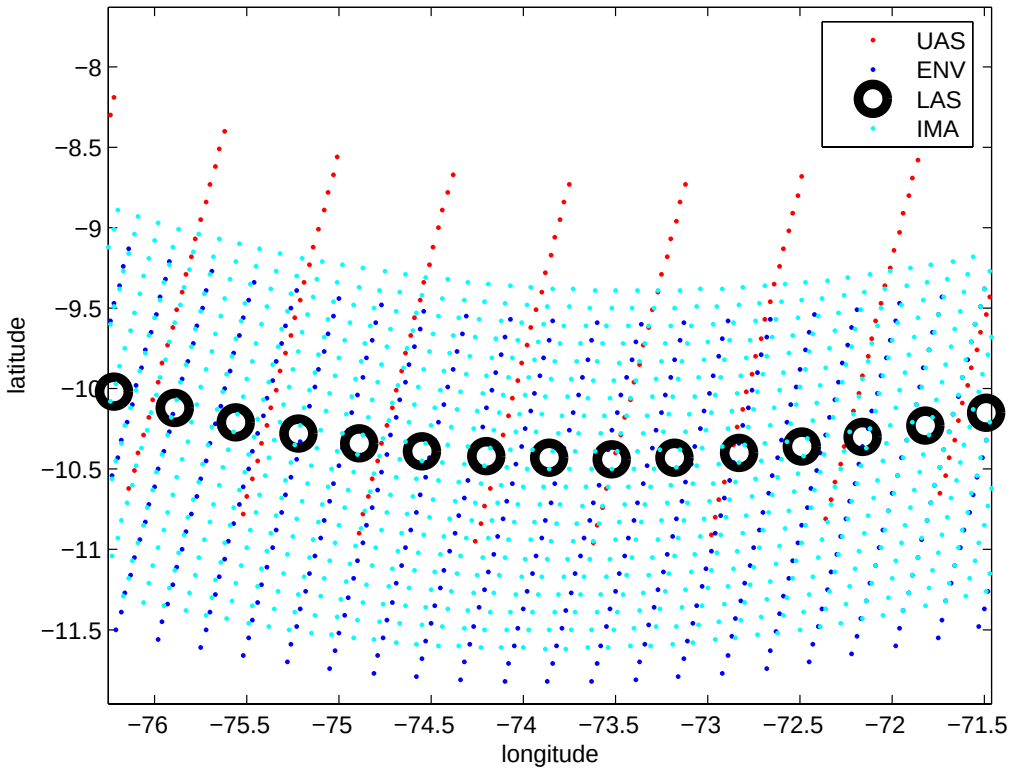

Figure 3: Centre positions of ground footprints for the four SSMIS instument subtypes. A section of one scan line for the lower atmospheric sounding scans is shown enlarged and in bold. The distance between adjacent scan lines is equal and constant for all subtypes (12.5km). The radiance field is heavily oversampled in the along track direction.

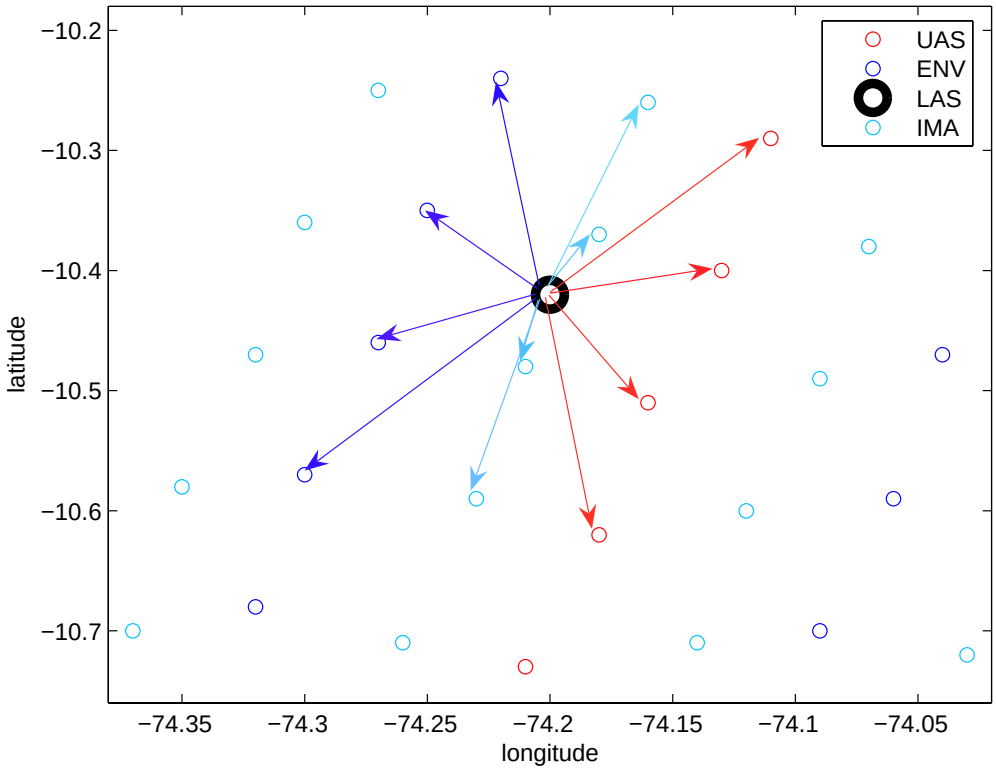

Figure 4: A section of the SSMIS swath showing the relative locations of LAS, UAS, ENV and IMA footprints. Remapping to the LAS footprints is carried out by taking a weighted average of the brightness temperatures from the four nearest neighbours for each of the three other subtypes as illustrated. The weighting is given by the inverse distance from the LAS footprint to each of the neighbours, normalised appropriately.

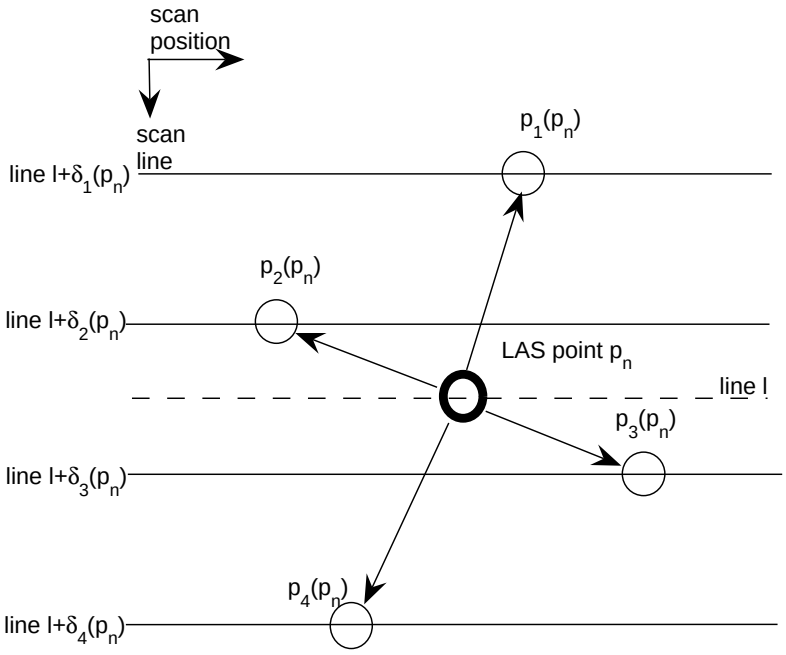

Figure 5: Schematic of the remapping scheme.

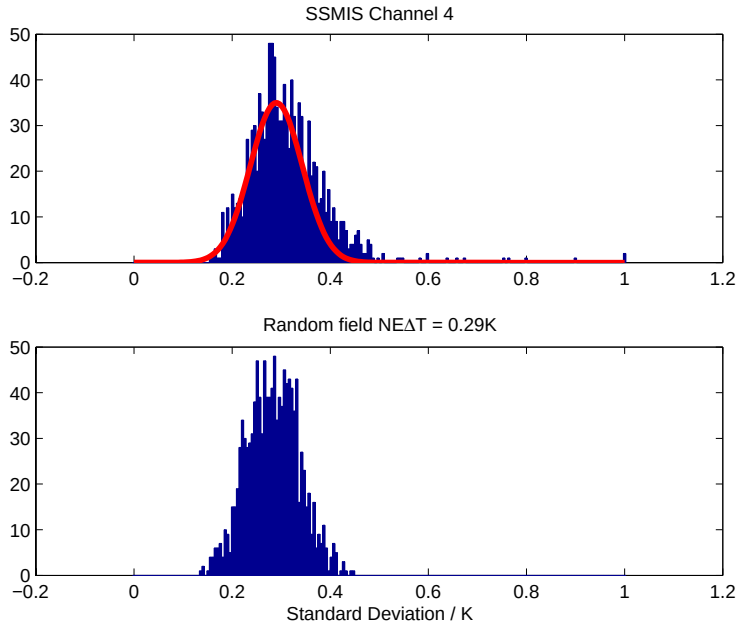

Figure 6: The distribution of computed standard deviations for the brightness temperatures from the central fifteen fields of view for SSMIS channels 4 (upper plot). Also shown, in red, is the distribution to be expected for a flat field with noise with a standard deviation of 0.29K. The curve is fitted iteratively using the low scatter end of the observed distribution, the asymmetry evident at the high end of the distribution results from the effect of real geophysical variability. The bottom curve shows the distribution to be computed from a synthetic flat field with noise added, with a standard deviation of 0.29K. This has been repeated for all lower atmospheric sounding channels and the results are summarised in Table 2.

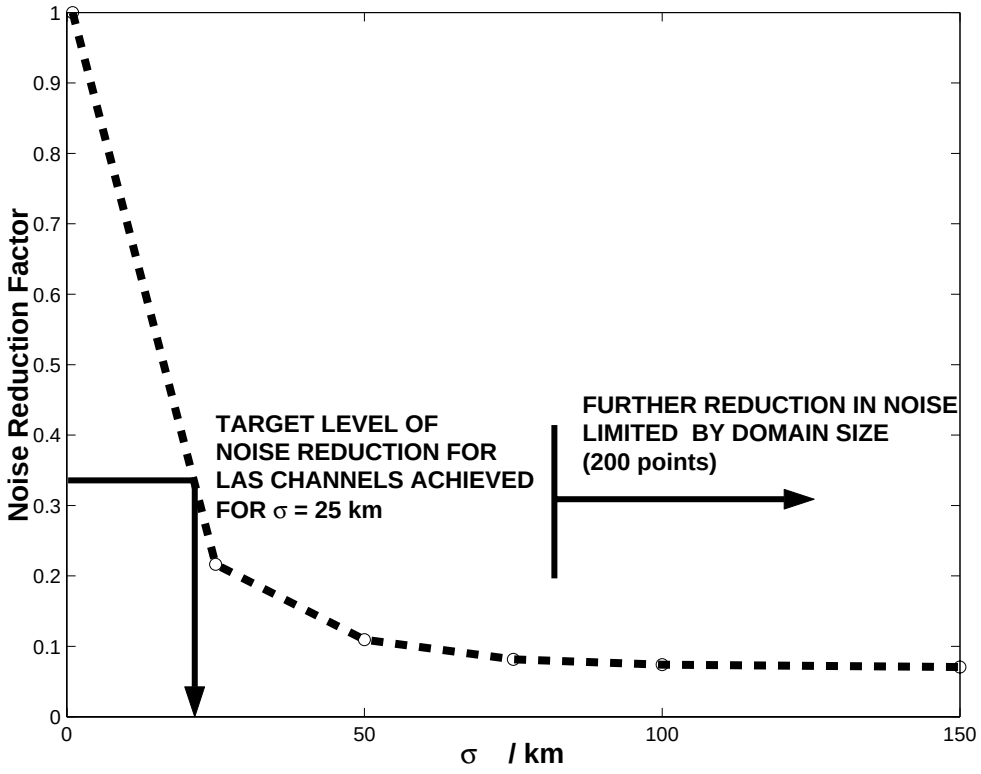

Figure 7: The reduction in noise levels as a function of σ. Assuming a target level of noise reduction of 0.33, which gives effective NEΔT values of 0.1K for the lower atmospheric sounding channels, this is achieved for averaging scales given by $\sigma > 25$km.

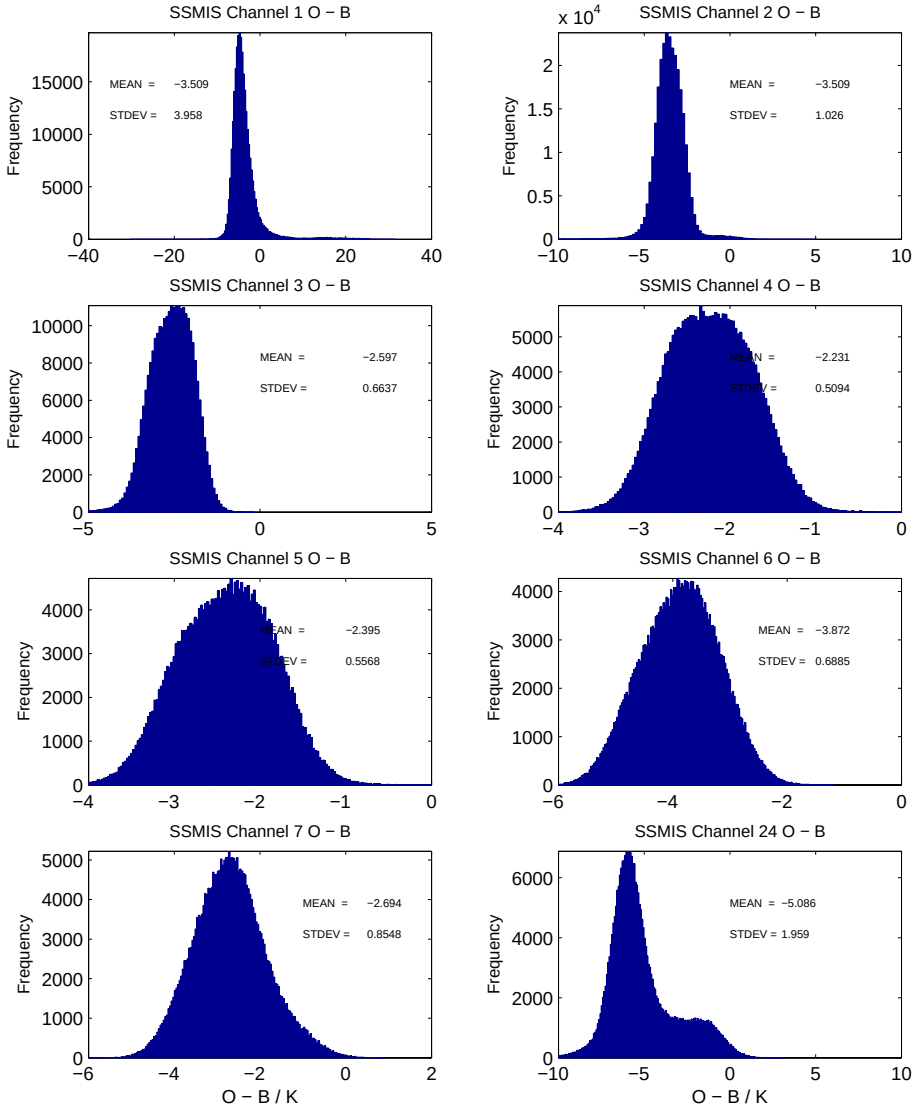

Figure 8: The distribution of computed innovations for the lower atmospheric sounding (LAS) channels 1-7 and 24. The standard deviations for channels 4,5,6 are in the range 0.5 - 0.8K, larger than expected from the known background errors and the estimated noise characteristics. For example for channel 4, assuming a background error standard deviation of 0.2K, together with estimated noise of 0.29K, a std of (O-B), assuming gaussian errors, should be 0.35K, but is computed to be 0.5K. Some additional source of error is contributing to the observed variance.

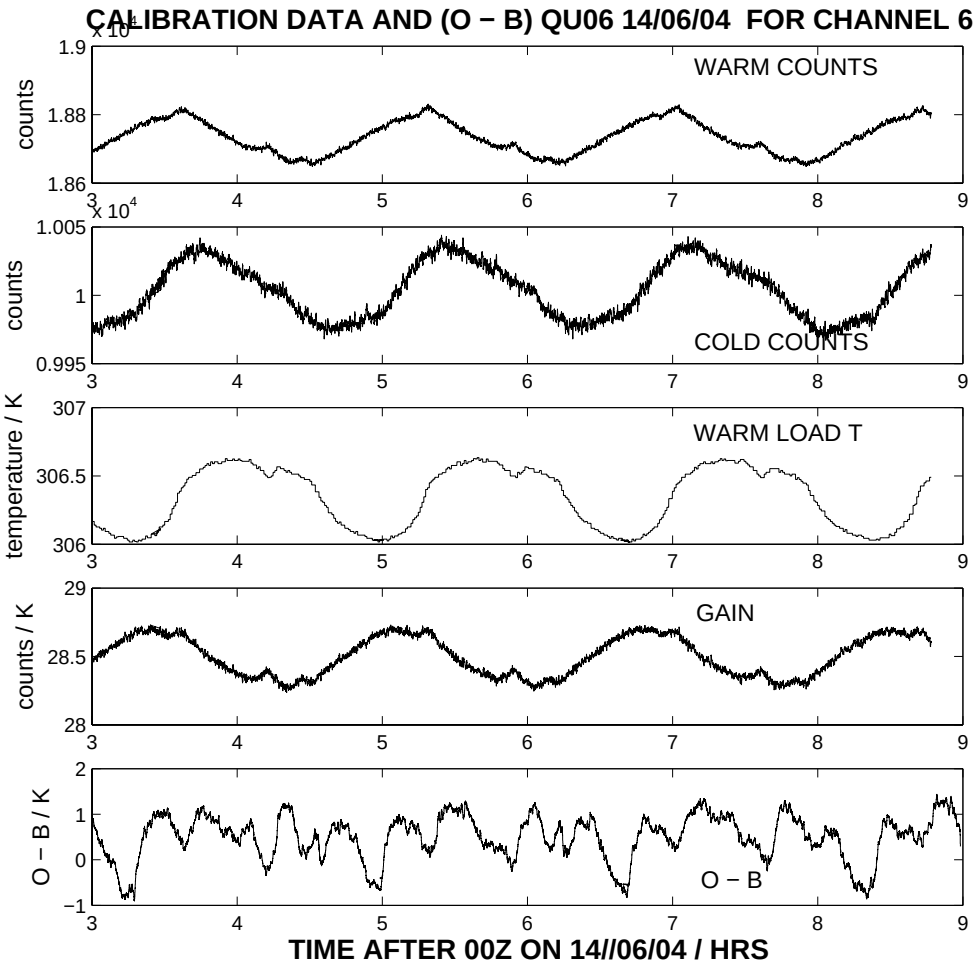

Figure 9: The calibration data for channel 6 over a six hour period, corresponding to approximately 3 orbits. Also shown is a time series of smoothed innovations for channel 6. The positive anomalies in the gain time series correlate strongly with the negative anomalies in the observations (and hence innovations). The magnitude of the negative departures in the innovations is in the range 1-1.5K and explains much of the observed variance in the computed innovations. The gain anomalies result from solar intrusions into the warm calibration load which cause transient heating of the warm load tines. This heating is not registered by the thermistors in the tine substrate material and this gives rise to the anomalously high gain.

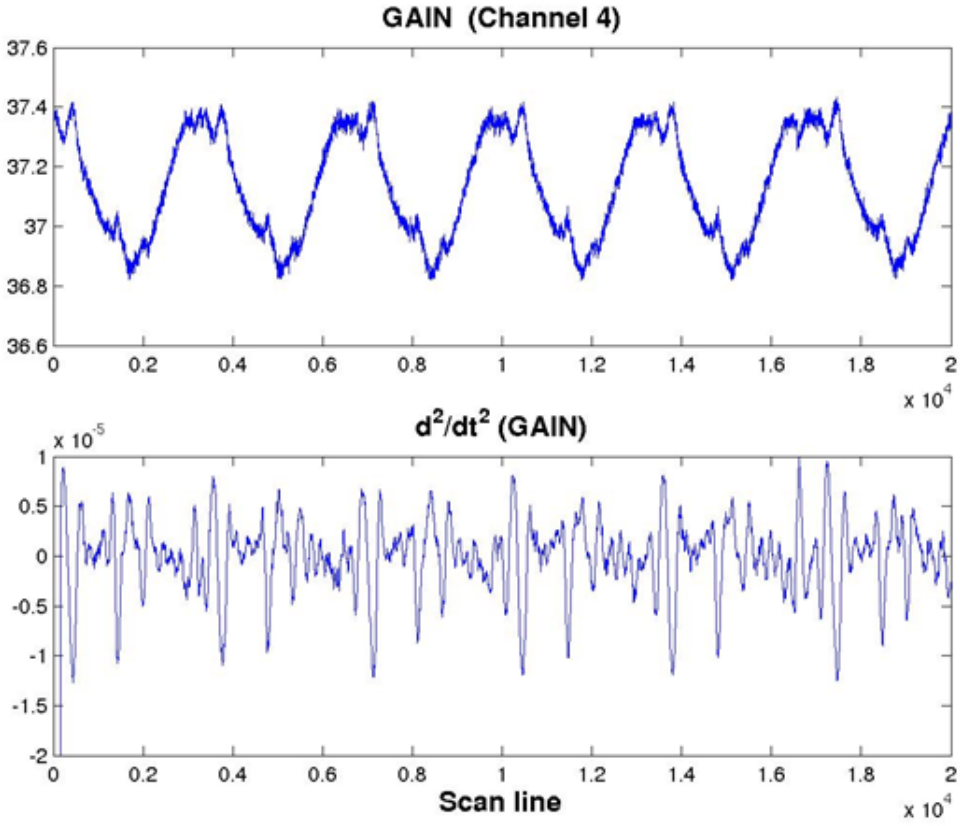

Figure 10: The upper panel shows the time evolution of the gain for channel 4. The lower panel shows the second derivative of the gain with respect to time. This has the effect of identifying the faster variations in gain due to solar intrusion effects from the slower natural variations round the orbit. Thresholds can be set to detect the intrusions in this way and a climatology of intrusions can be generated.

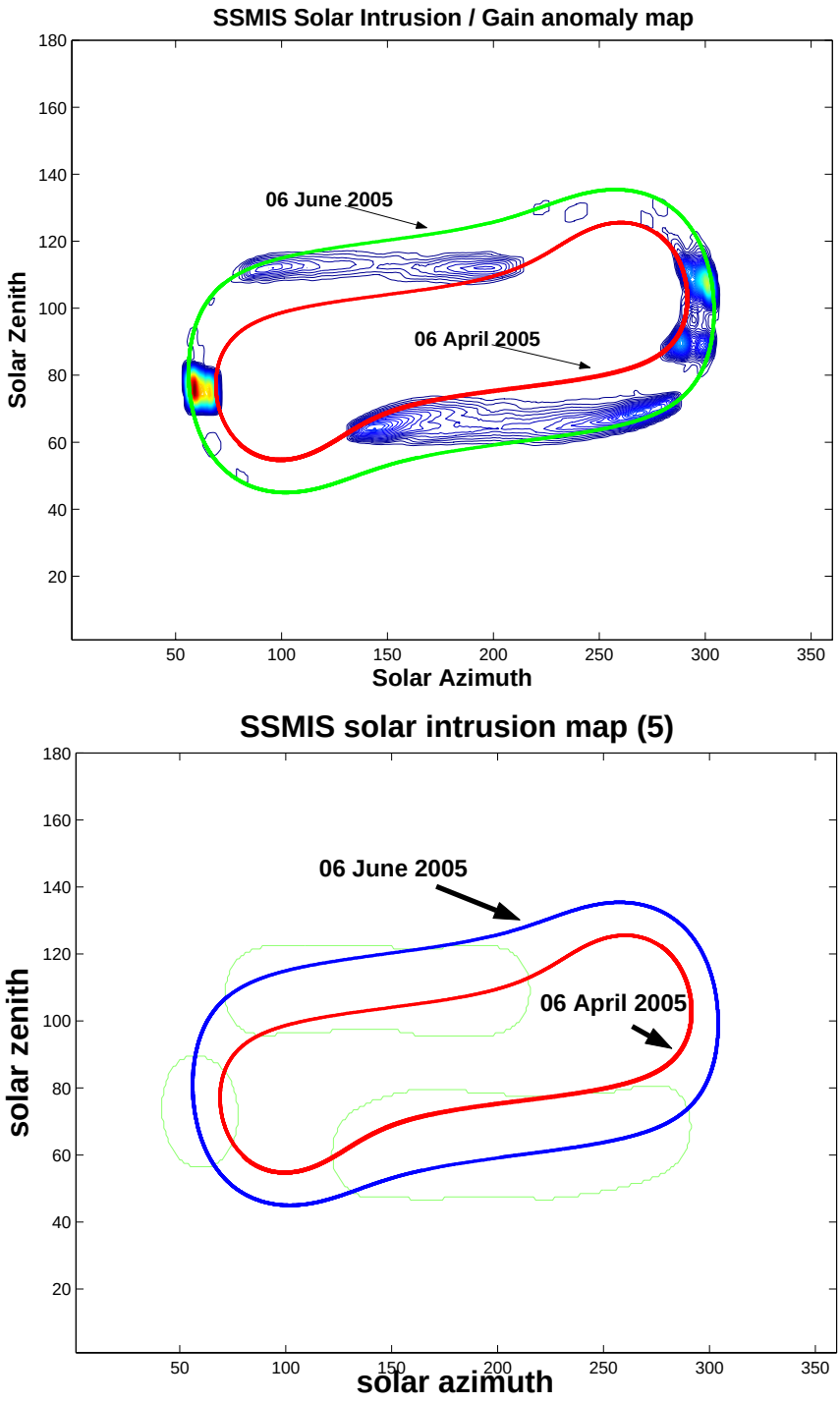

Figure 11: (Top) The climatological map of the solar intrusions constructed from the time series of computed gains. (Bottom) The final version of the map (green) computed by smoothing the original map(top) by 2D convolution with a gaussian weighting function . The trajectories of the Sun in the space defined by the local solar zenith and azimuth angles are shown for 6th April 2005 and 6th June 2005 .

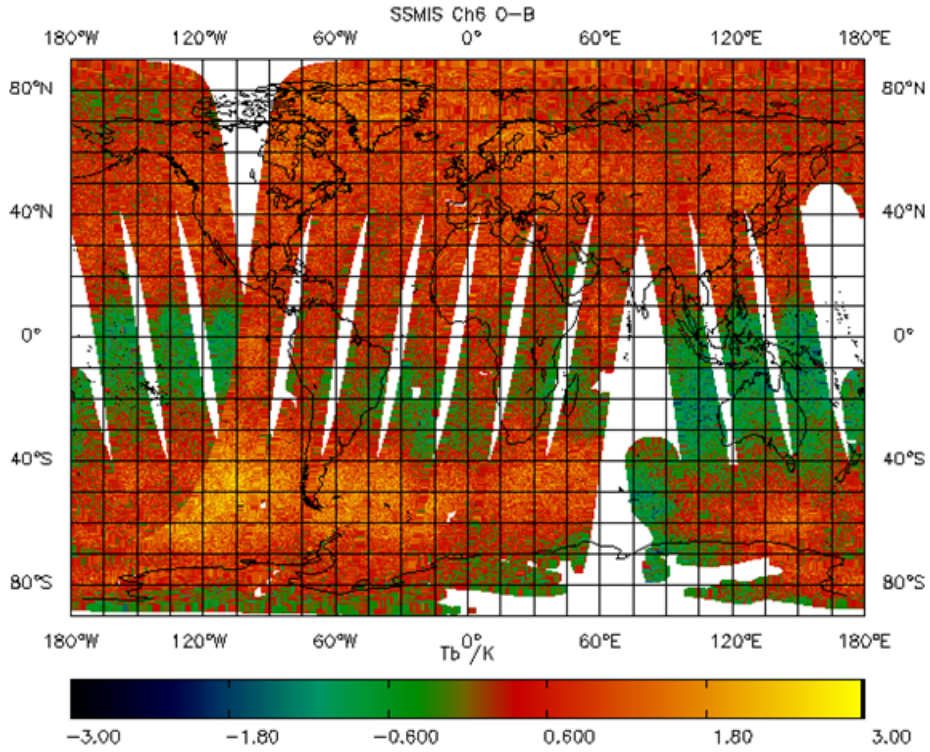

Figure 12: The innovation map computed for channel 6 for a 12 hour period during 14/06/05. The step change due to reflector emission on emergence from earth shadow is evident in the northbound ascending node, just north of the equator.

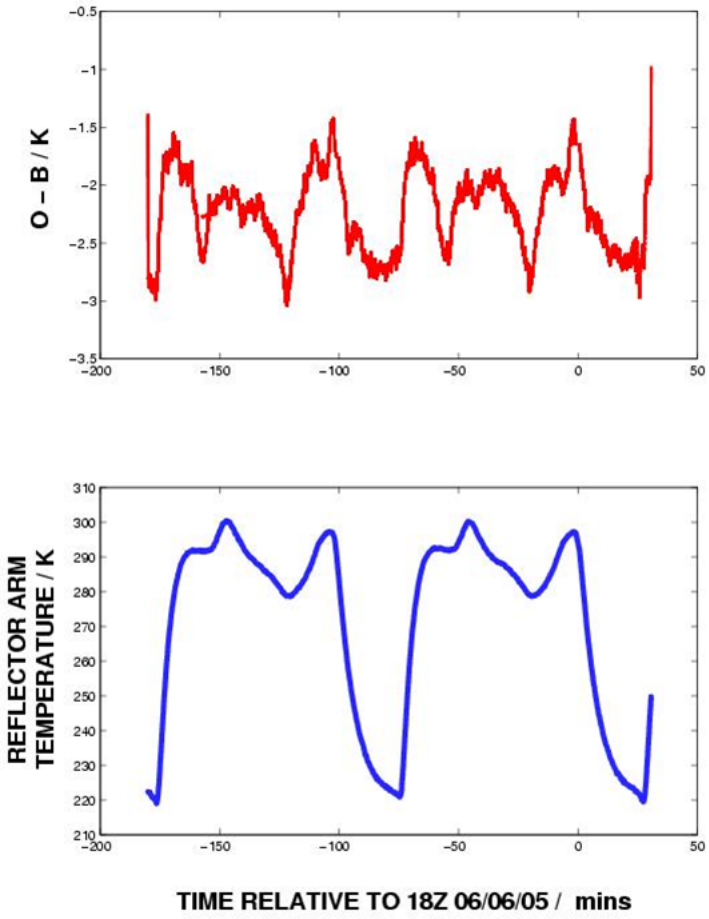

Figure 13: (Top) Time series of innovations for channel 4 over two orbits showing the step change in innovations. The lower plot shows the evolution of the reflector arm temperature over the same period, showing the 80K increase in reflector arm temperature over a period of less than 10 minutes, coincident with the step change in the compute innovations.

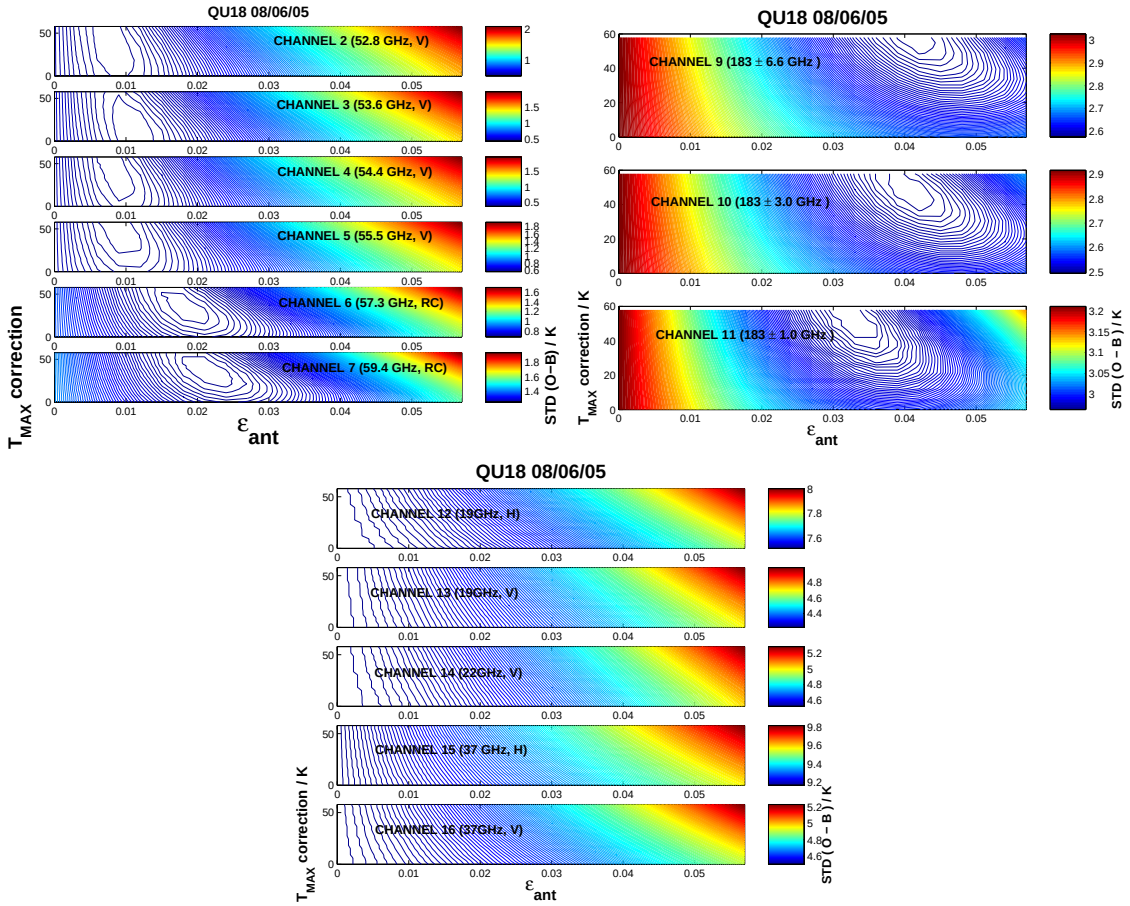

Figure 14: The fit of observed radiances to Met Office background fields as a function of assumed emissivity and maximum amplitude of the temperature correction (the maximum amplitude of the second term in the RHS of equation 9) to the reflector temperature for channels 2-7 (top left), channels 9-11 (top right) and channels 12-16 (bottom).

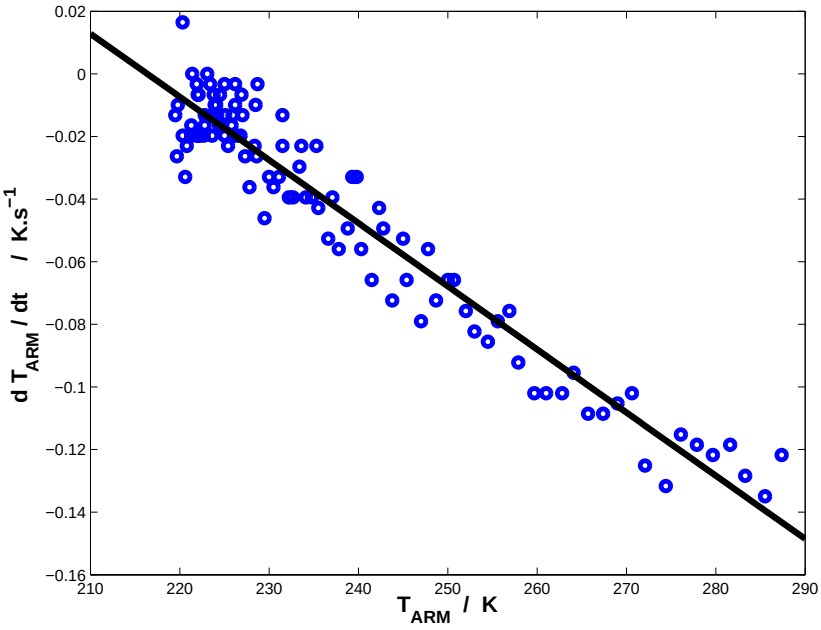

Figure 15: Gradient of reflector arm temperature with respect to time versus arm temperature, demonstrating that the arm is cooling conductively.

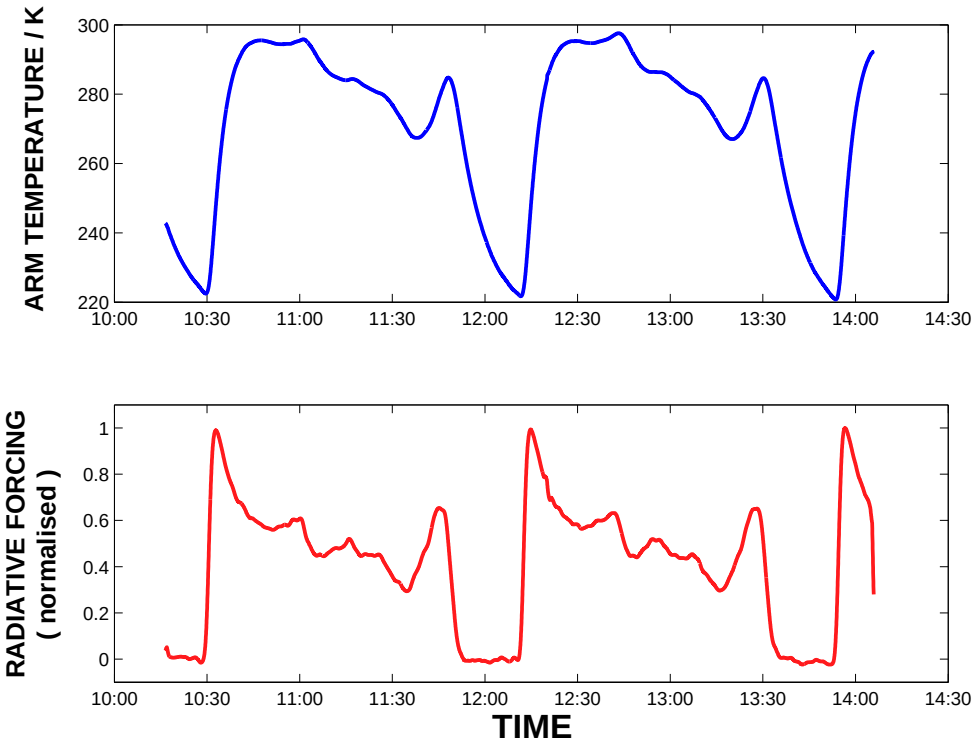

Figure 16: Constructed radiative forcing, derived from the form of the time evolution of the arm temperature.

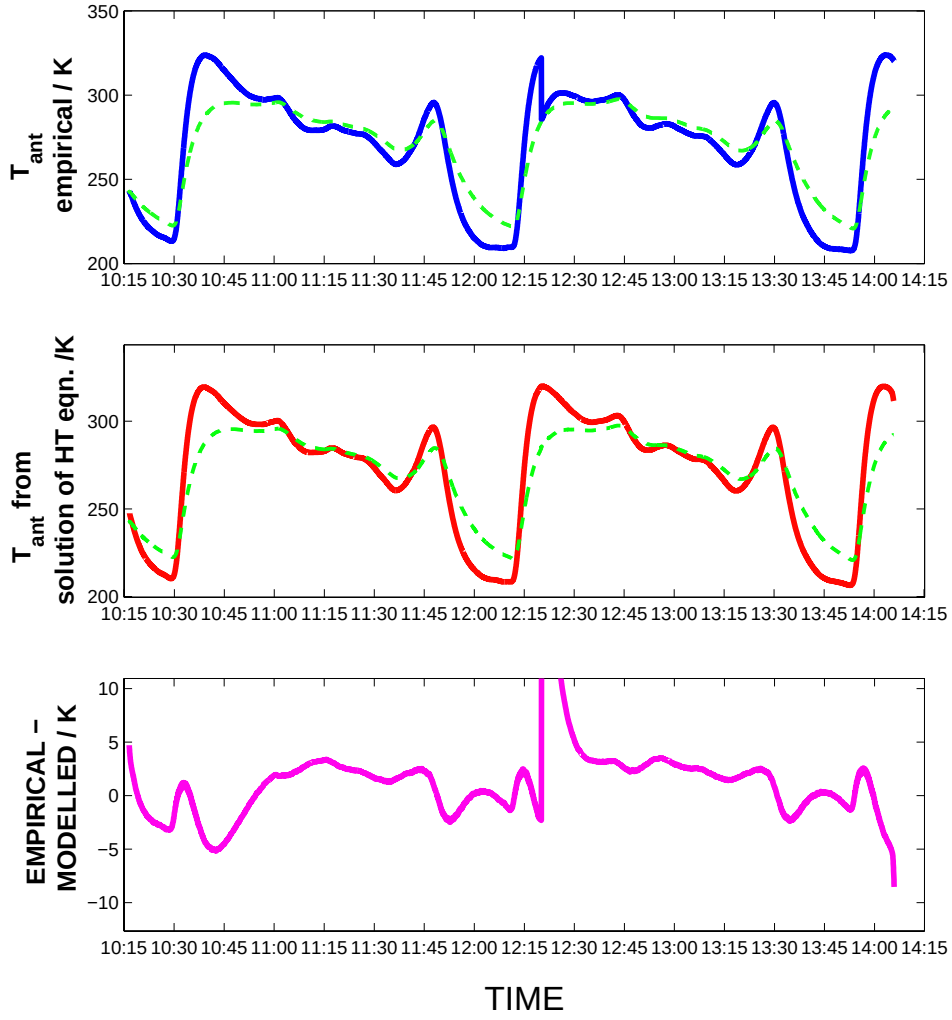

Figure 17: Comparison of numerical solution of heat transfer equation versus the empirical correction for a choice of reflector thermal properties.

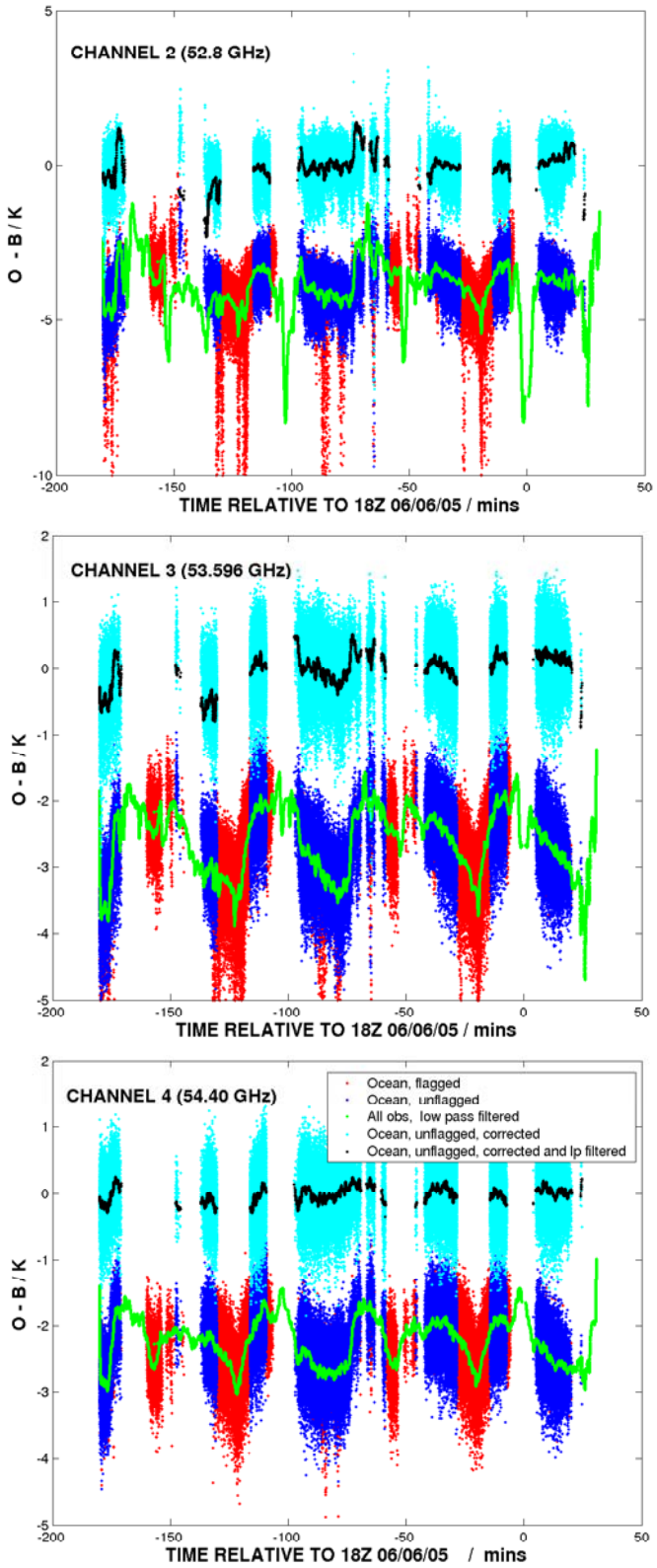

Figure 18: Performance of the corrections for channels 2,3 and 4. For clarity the smoothed timeseries of innovations for all uncorrected observations is shown in green. The smoothed timeseries of corrected observations for unflagged ocean observations is shown in black. Individual corrected unflagged ocean observations areshown in light blue. Individual flagged and uncorrected observations are shown in red. Individual unflagged uncorrected ocean observations ae shown in dark blue.

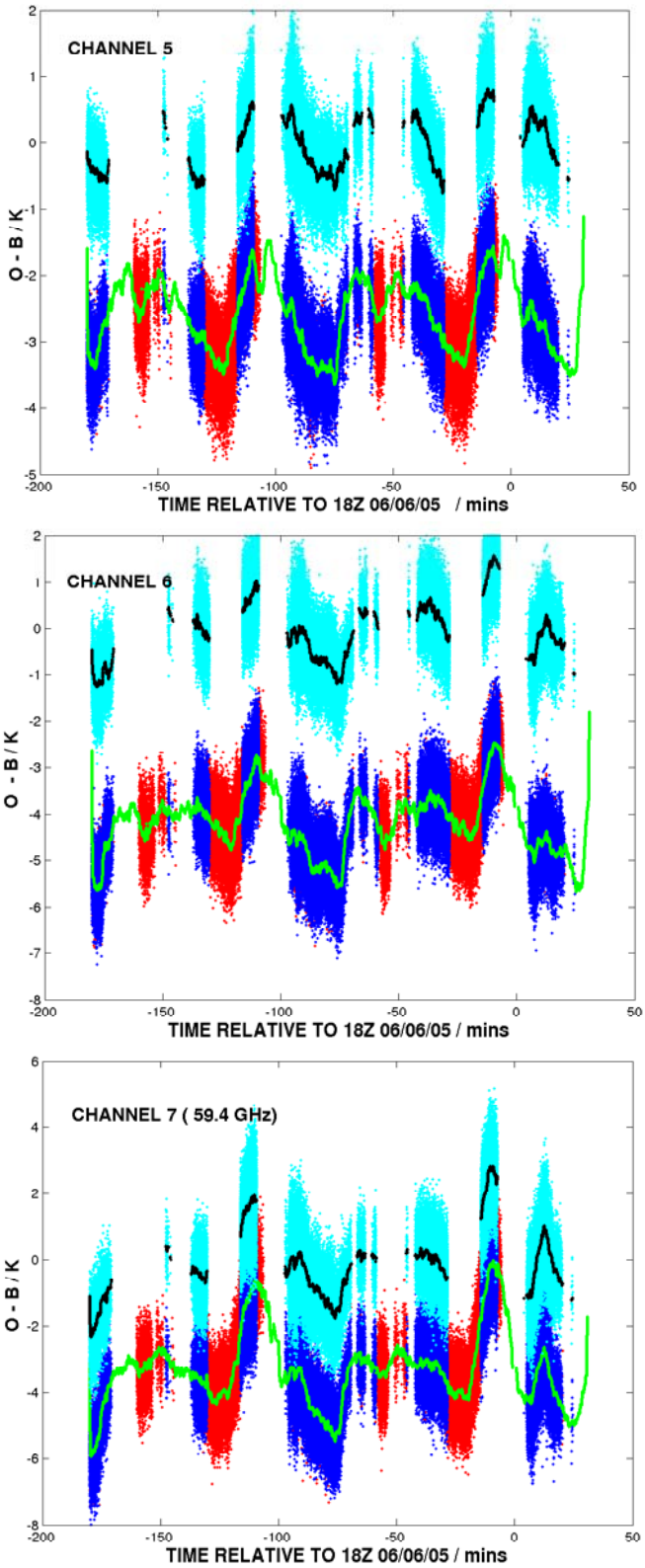

Figure 19: Performance of the corrections for channels 5,6 and 7 (see previous figure for key)

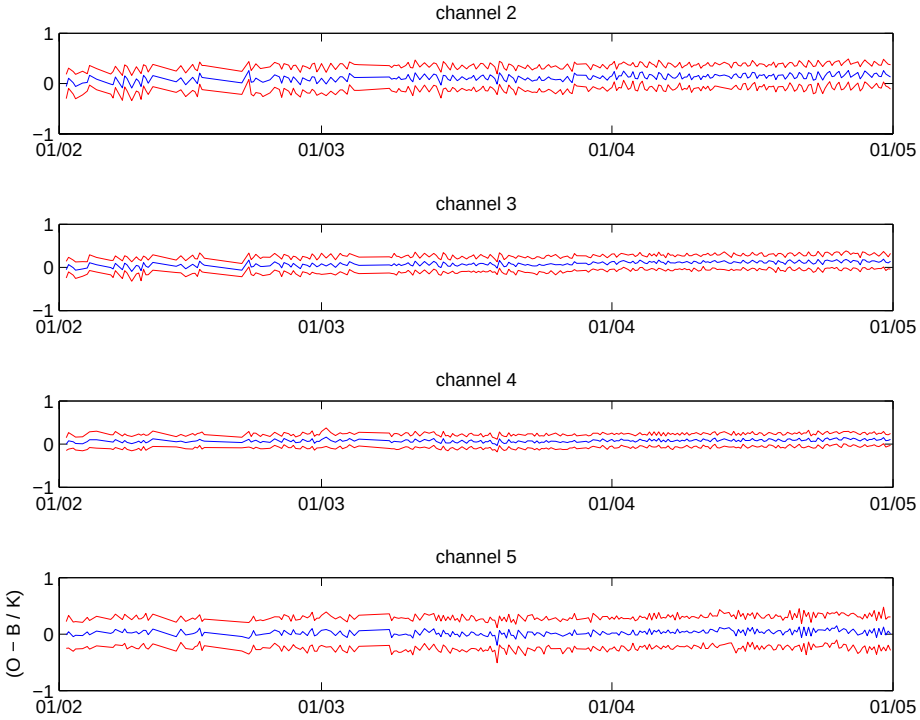

Figure 20: Mean (blue) and standard deviation (red) for bias corrected innovations calculated during the period 1st February - 1st May 2006 for channels 2-5.

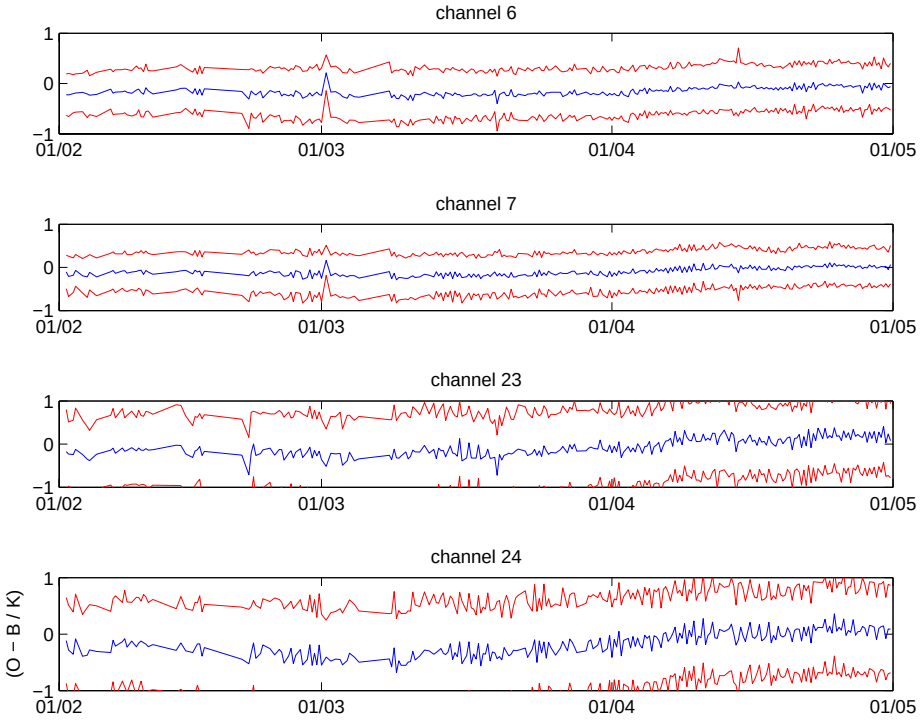

Figure 21: Mean (blue) and standard deviation (red) for bias corrected innovations calculated during the period 1st February - 1st May 2006 for channels 6,7, 23 and 24.

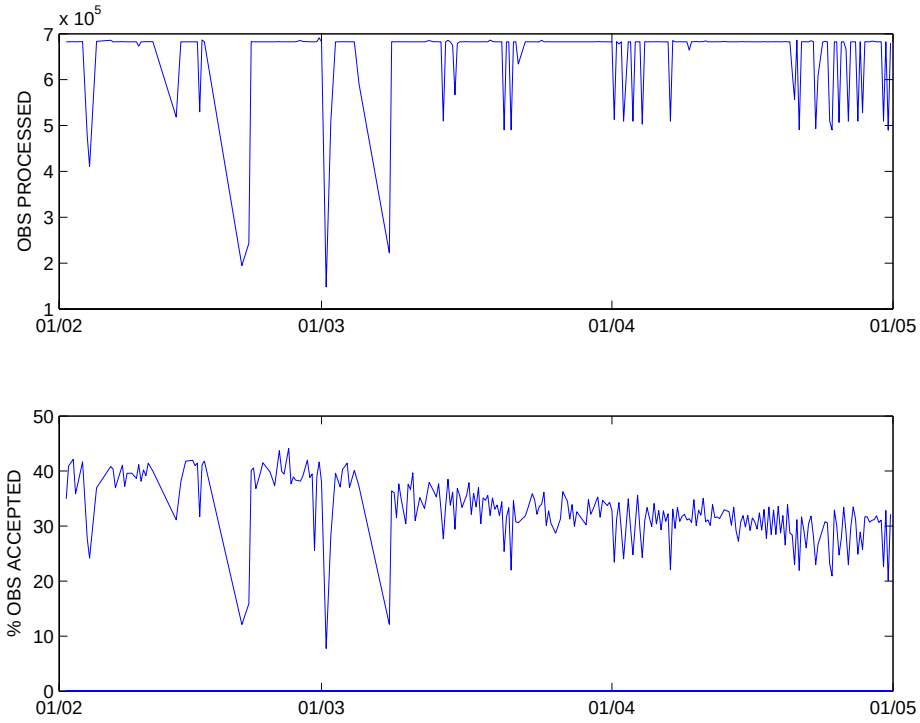

Figure 22: The top plot shows the number of observations processed in each 6 hour assimilation window during the period 1st Februiary - 1st May 2006. The intermittant outages are due mainly to local issues related to the processing running on low priority non-operational queues, as well as local storage problems. The lower plot shows the percentage of these observations passing QC check in 1D Var. The most significant rejections are due to rain/intrusion flagging (40 - 60%) and non-convergence of the 1D Var analysis (10%)

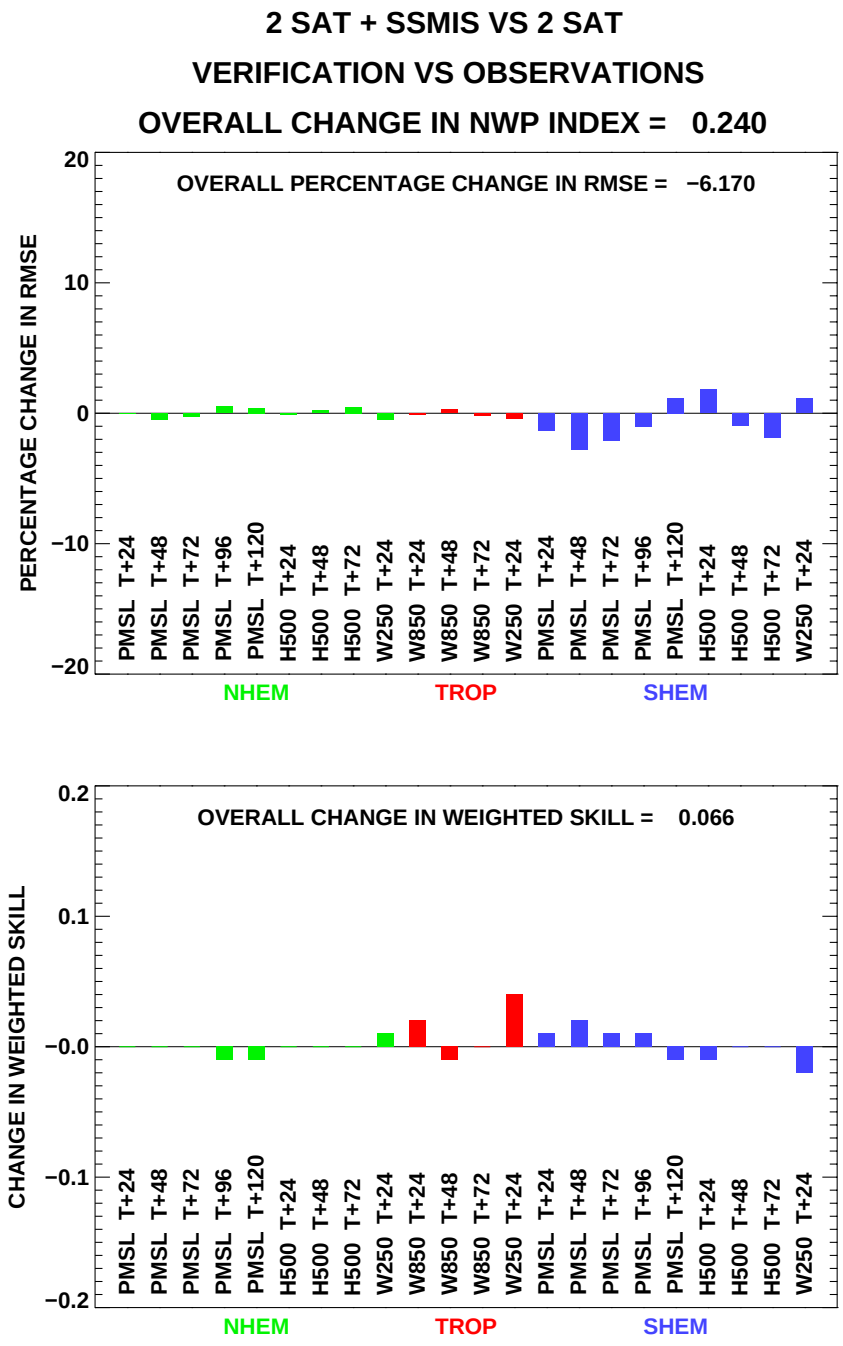

Figure 23: Impact of including SSMIS radiances from the lower atmospheric temperature sounding channels on forecast variables in the NH, Tropics and SH. The most significant impacts are in the SH where Day 1-3 forecast errors for PMSL are improved by 1-2.5 %. This experiment assumed a baseline assimilation system including two NOAA AMSU-A instruments : NOAA-16 and NOAA-18.

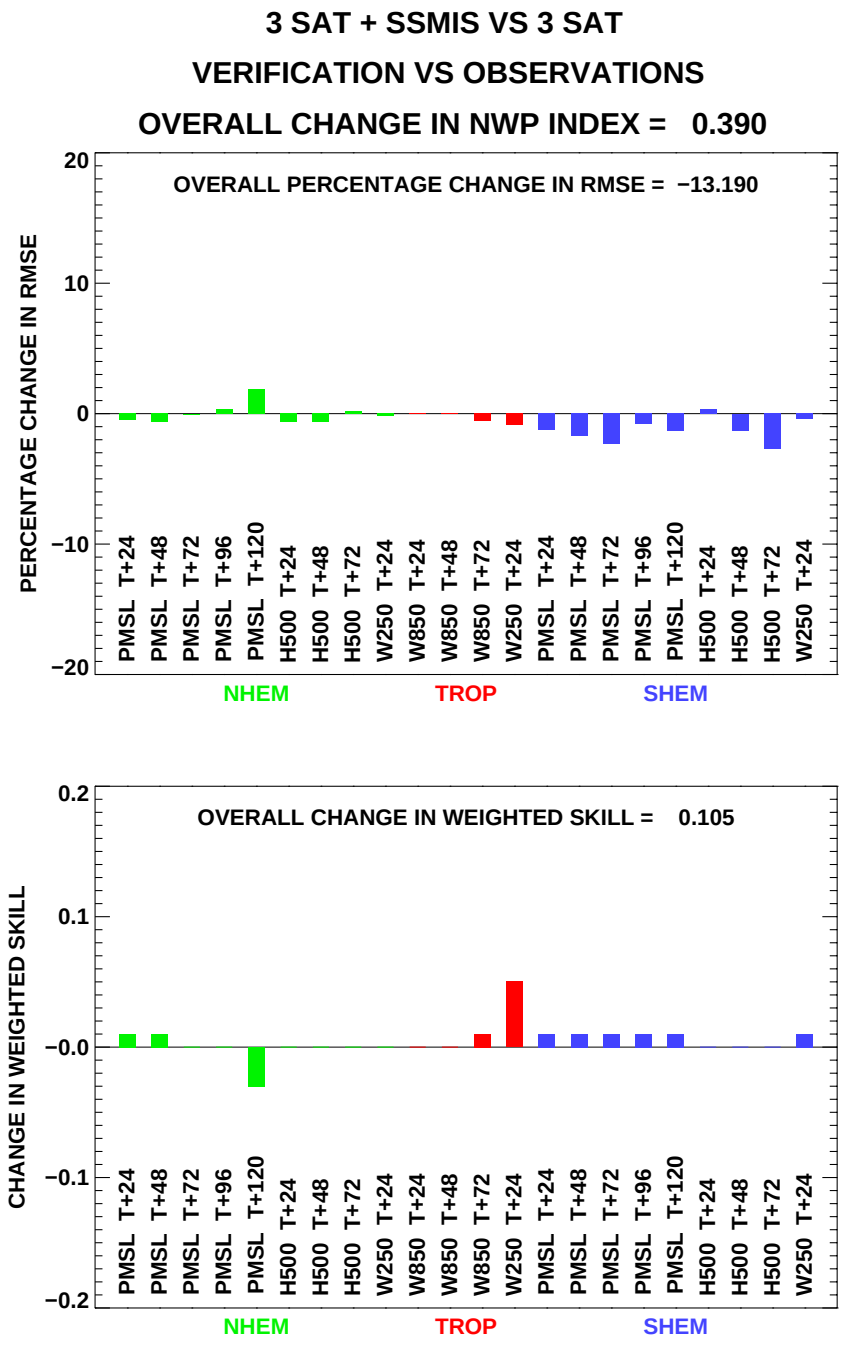

Figure 24: Impact of including SSMIS radiances from the lower atmospheric temperature sounding channels on forecast variables in the NH, Tropics and SH. The most significant impacts are in the SH where Day 1-5 forecast errors for PMSL are improved by 1-2.5 %. This experiment assumed a baseline assimilation system including three NOAA AMSU-A instruments : NOAA-15, NOAA-16 and NOAA-18.